ADVANCED OPTICAL MATERIALS
www.advopticalmat.de

# Vapor-Phase Growth of $CsPbBr_3$ Microstructures for Highly Efficient Pure Green Light Emission

*Shangui Lan, Wancai Li, Shuai Wang, Junze Li, Jun Wang, Haizhen Wang, Hongmei Luo, and Dehui Li**

**All-inorganic lead halide perovskites have been extensively studied in the past several years due to their superior stability against moisture, oxygen, light, and heat compared with their organic–inorganic counterparts. $CsPbBr_3$ with suitable band gap and ultrahigh photoluminescence quantum yield is a promising candidate for pure green emitter in the backlighting display to fill the so-called "green gap." Here, vapor-phase growth of $CsPbBr_3$ microspheres is reported for highly efficient pure green light emission. The as-synthesized microspheres exhibit a stronger photoluminescence (PL) intensity with a photoluminescence quantum yield of 75% resulting from the lower energy of longitudinal optical phonons revealed by temperature dependent PL studies. Importantly, with the diameter increasing from 2 to 50 µm the PL peak positions of the microspheres can be readily tuned from 527 to 539 nm, well filling the so-called "green gap." The red-shift with increasing diameter can be ascribed to the reabsorption process during the photon propagation inside the microspheres. The studies provide a route to improve the photoluminescence quantum yield in all-inorganic lead halide perovskites, but also suggest an alternative approach to achieve the pure green emission for the backlighting display.**

## 1. Introduction

In the past several years, organic–inorganic lead halide perovskites (OILHPs) have been extensively studied due to their excellent optoelectronic properties.[1–4] Their long carrier diffusion length,[2] moderate carrier mobility,[3] high photoluminescence quantum yield (PLQY)[4] as well as high defect tolerance[5] make them ideal materials for diverse optoelectronic applications, such as photovoltaics, photodetectors, light emitting diodes, and lasers.[4,6–8] In particular, OILHPs-based solar cells have achieved a certified power conversion efficiency of over 22% in just a few years.[6] Nevertheless, despite the unprecedented advances of the OILHPs-based solar cells, their inherent environment instability hinders their commercialization due to the presence of hydrophilic organic cations ($MA^+$ or $FA^+$). Compared with OILHPs, all inorganic lead halide perovskites (for example, $CsPbBr_3$) without hydrophilic organic groups exhibit superior stability against moisture, oxygen, light, and heat, and thus have attracted increasing attention recently.[9] All inorganic lead halide perovskite based solar cells,[10] photodetectors,[11] light emitting devices,[12] and lasers[13] have been demonstrated with a respectable performance. Especially, all inorganic lead halide perovskites possess extremely high photoluminescence quantum yield, which makes them as promising materials for next-generation display.[14]

To reproduce the object colors for a backlighting display, it is essential to obtain a wider color gamut with ultrapure emission. While the red emitters have been well developed, there is only weakly emitting in blue and no true green emission (525–535 nm) has been achieved, which is critical to replicate high quality white light display since human eyes are extremely sensitive to green light.[15] $CsPbBr_3$ is a potential candidate to close the so-called "green gap" due to its suitable band gap and ultrahigh PLQY.[16,17] Nevertheless, $CsPbBr_3$ bulk thin films are able to only emit a blue-green color light (≈520 nm) while $CsPbBr_3$ quantum dots exhibit a blueshifted emission wavelength due to quantum confinement effect, both of which cannot truly replicate the green emission.[12] Yu et al. have successfully demonstrated ultrapure green emission with high PLQY in formamidinium perovskite nanoplates at the sacrifice of the long-term stability due to the presence of the organic cations.[16] Recently, spontaneously self-assembled $CsPbBr_3$ supercrystals have been achieved with emission wavelength around 530 nm, which is believed to be able to fill the green gap.[17] Nonetheless, the assembled supercrystals suffer from the partial disassembly in the diluted solution during the following device fabrication process, which would lead to the shift and broadening of the emission peak.[17] To this end, it

S. Lan, W. Li, S. Wang, J. Li, Dr. J. Wang
School of Optical and Electronic Information
Huazhong University of Science and Technology
Wuhan 430074, China
H. Wang, Prof. H. Luo
Department of Chemical and Materials Engineering
New Mexico State University
NM 88003, USA
Prof. D. Li
School of Optical and Electronic Information and Wuhan National Laboratory for Optoelectronics
Huazhong University of Science and Technology
Wuhan 430074, China
E-mail: dehuili@hust.edu.cn
The ORCID identification number(s) for the author(s) of this article can be found under https://doi.org/10.1002/adom.201801336.

DOI: 10.1002/adom.201801336

is urgent to explore alternative route to obtain $CsPbBr_3$ with great stability to truly replicate the pure green emission for displays.

Here, we report on vapor-phase growth of $CsPbBr_3$ microspheres for highly efficient pure green light emission. We can controllably synthesize $CsPbBr_3$ microplates (cubic phase), pyramids (monoclinic phase), and microspheres (monoclinic phase) by conveniently tuning the growth conditions including the cooling rate and growth time. The synthesized microspheres exhibit a stronger PL intensity compared with the pure $CsPbBr_3$ microplates and pyramids due to the smaller energy of longitudinal optical (LO) phonons. With the diameter increasing from 2 to 50 μm, the PL peak positions are redshifted from 527 to 539 nm due to the reabsorption effect, making the microspheres promising for pure green light emitters. In particular, we estimated the PLQYs of various microstructures and demonstrated that the PLQYs of microspheres with pure green emission can achieve as high as 75%, which is the highest number for the pure green light emission of perovskites. It is the first time to understand the underlying mechanism for the different PLQYs for different morphologies of $CsPbBr_3$ microstructures and achieve pure green emission with a highest PLQYs from $CsPbBr_3$ microspheres grown by vapor phase growth.

## 2. Results and Discussion

The synthesis of $CsPbBr_3$ microstructures was carried out by one-step method in a home-built vapor transport chemical vapor deposition system,[18,19] schematic illustration of which is displayed in **Figure 1**a. CsBr and $PbBr_2$ powder with molar ratio of 1:1 were mixed and placed at the center of the tube furnace. After pumped down and purged by Argon gas for several times, the tube was then heated to 570 °C, maintained at this temperature for different time and finally cooled to room temperature with different cooling rate to obtain $CsPbBr_3$ microstructures with different morphologies. With the same growth time of 5 min, either microplates or pyramids are able to be obtained by properly tuning the cooling rate. If the lid of furnace is opened at 500 °C (corresponding to a cooling rate of ≈40 °C $min^{-1}$), $CsPbBr_3$ microplates can be grown (Figure 1b,e) while $CsPbBr_3$ pyramids are synthesized (Figure 1c,f) if the lid is opened at 300 °C (corresponding to a cooling rate of ≈20 °C $min^{-1}$). The optical and scanning electron microscopy (SEM) images indicate that microplates (Figure 1b,e) and pyramids (Figure 1c,f) possess rather smooth surface and sharp edge with a lateral size on the order of tens of micrometers, suggesting their excellent crystalline quality. In contrast, if the growth time is prolonged to 40 min and the cooling rate maintains at ≈40 °C $min^{-1}$, $CsPbBr_3$ microspheres are achieved with fairly uniform distribution. Nevertheless, unlike the microplates and pyramids, the surface of the microspheres is relatively rough, revealing the polycrystalline nature of the as-grown microspheres (Figure 1d,g). The diameter of the microspheres also has a wider distribution in the range of tens of micrometers. It should be noted that the diameter of microspheres can be continuously tuned by changing the distance between the precursor and the position of the substrate placed, which will be discussed in detail below.

**Figure 2**a displays the powder X-ray diffraction (PXRD) patterns of the microplates and pyramids. The XRD pattern of microplates exhibits a narrow full width at half maximum

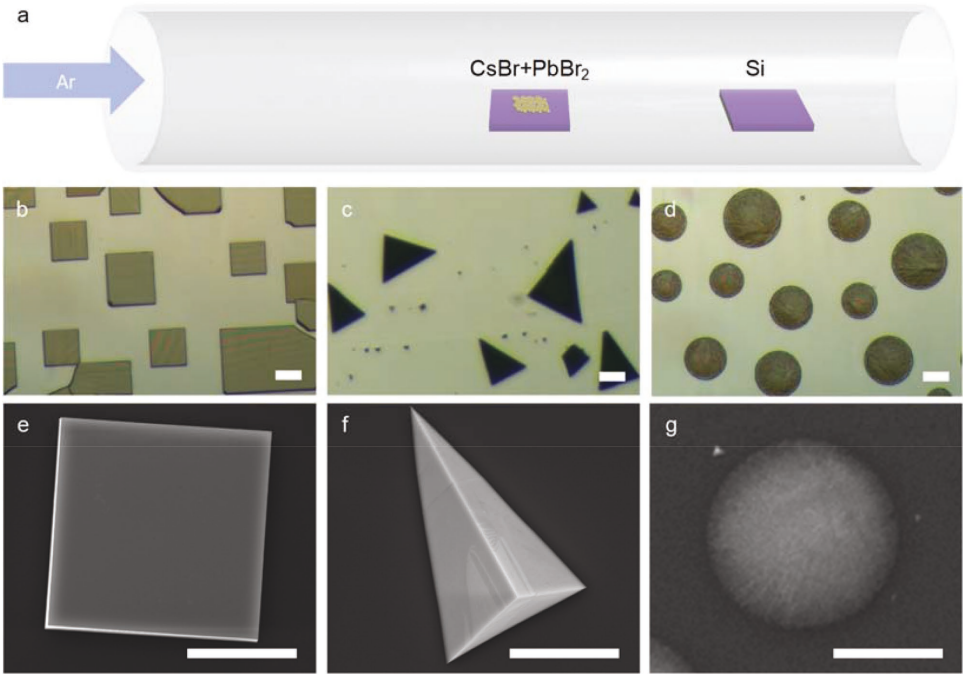


**Figure 1.** a) Schematic diagram of experimental setup. b,c,d) Optical and e,f,g) scanning electron microscopy (SEM) images of the as-grown $CsPbBr_3$ b,e) microplates, c,f) pyramids, and d,g) microspheres. The scale bar is 10 μm for all optical and SEM images.

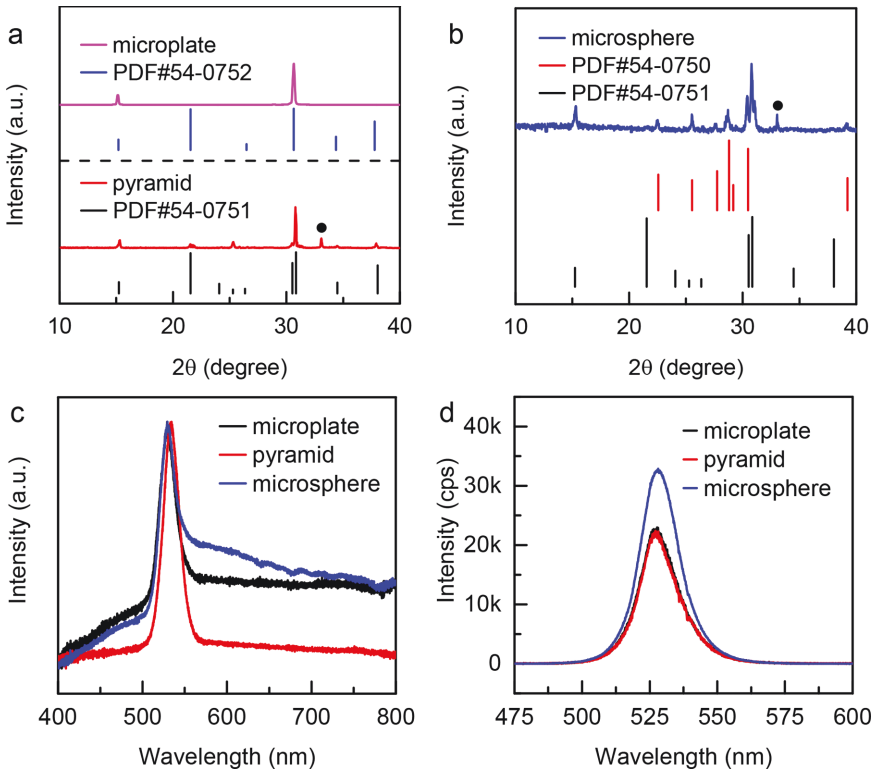


**Figure 2.** a) X-ray diffraction (XRD) patterns of microplates (pink line) and pyramids (red line), corresponding to cubic (PDF#54-0752) and monoclinic (PDF#54-0751) phase. b) The XRD pattern of microspheres contains the diffraction peaks of $CsPbBr_3$ (PDF#54-0751) and $Cs_4PbBr_6$ (PDF#54-0750). The black solid dots indicate the diffraction peaks of Si substrate. c) Reflection spectra of microplates (black line), pyramids (red line), and microspheres (blue line). d) Room temperature steady-state photoluminescence (PL) spectra of microplates (black line), pyramids (red line), and microspheres with diameter of ≈2 µm (blue line). The spectra are collected under the same conditions.

(FWHM) and high signal-to-noise ratio suggesting the good crystalline quality of the as-grown microplates. All diffraction peaks of microplates can be indexed to the cubic phase (PDF#54-0752) of $CsPbBr_3$, which reveals that the as-synthesized microplates have cubic structure. In contrast, two diffraction peaks close to (200) peak of microplates are present for pyramids (Figure 2a) and microspheres (Figure 2b), which can be assigned to the (210) and (002) peaks of $CsPbBr_3$ monoclinic phase (PDF#54-0751), suggesting that $CsPbBr_3$ pyramids and microspheres exhibits monoclinic phase rather than cubic phase. In addition, there are a few extra peaks, which match well with the diffraction peaks of orthorhombic phase of $Cs_4PbBr_6$ (PDF#54-0750), implying the microspheres are mixture of $CsPbBr_3$ and $Cs_4PbBr_6$. The different phases for different morphologies might be originated from the phase transition kinetics from high-temperature phase to low-temperature phase of $CsPbBr_3$. In general, cubic phase $CsPbBr_3$ is stable only at temperature higher than 133 °C and undergoes a phase transition to low-temperature phases (monoclinic, tetragonal, and orthorhombic) below 133 °C. Nevertheless, the $CsPbBr_3$ microplates with cubic phase can still be achieved and stable at room temperature if the cooling rate during the synthesis process is fast enough because of the slower phase transition kinetics.[19,20] We compared the $CsPbBr_3$ microstructures grown at a cooling rate of 40, 30, and 20 °C $min^{-1}$ as shown in Figure S1 in the Supporting Information. At the cooling rate of 30 °C $min^{-1}$, $CsPbBr_3$ microplates and pyramids can coexist, indicating that the phase transition is of first-order, similar to $MAPbI_3$.[21] Due to the slow first-order phase transition kinetics, the $CsPbBr_3$ microplates with cubic phase can still be achieved and stable at room temperature if the cooling rate during the synthesis process is fast enough (40 °C $min^{-1}$). In terms of the presence of $Cs_4PbBr_6$ within $CsPbBr_3$, it might be due to the different partial pressure of CsBr and $PbBr_2$,[22] leading to the fact that a longer growth time (40 min vs 5 min) favors introducing extra CsBr precursor and thus $Cs_4PbBr_6$ phase. For a longer growth time, the pregrown single crystal microplates evolve toward the polycrystalline microspheres.

We have carried out steady-state reflection and PL spectra of all three morphologies under the same conditions to check how morphologies and phases affect the optical properties of $CsPbBr_3$ microstructures. The reflection peaks for those three different morphologies almost coincide with the peak position of ≈2.4 eV, which is consistent with previous studies,[23] suggesting that the phase change and the presence of $Cs_4PbBr_6$ would not substantially alter the band gap energy of $CsPbBr_3$ microstructures (Figure 2c). This is further confirmed by the room-temperature steady-state PL spectra, which show same emission peak position for all three different morphologies (Figure 2d). Nevertheless, the PL intensity of microspheres for various diameters is higher than those of microplates and pyramids (Figure 2d). We have also measured the PLQYs of $CsPbBr_3$ microplates, pyramids, and microspheres. We used CdSe quantum dot films with a known PLQY to calibrate our measurement system and then evaluate the PLQYs of our samples. It is shown that the average PLQYs of microplates, pyramids, and microspheres are ≈55%, ≈55%, and ≈75%, respectively. It is much unexpected since it is believed that the presence of $Cs_4PbBr_6$ in microspheres would introduce extra ground boundaries and thus deteriorate the PL emission although the high PLQYs of 77% and 95% have been observed in $CsPbBr_3$ nanowires and quantum dots.[24,25,31]

To understand the origin of the enhancement of PL intensity in $CsPbBr_3$ microspheres, we have conducted the temperature-dependent PL measurement for these three different morphologies from 77 K to room temperature. **Figure 3**a–c show the temperature-dependent normalized PL spectra of microplates, pyramids and microspheres with diameter of ≈2 µm, respectively. The spectra are shifted vertically against each other for clarity. As seen from Figure 3a–c, there is only one emission peak in all the PL spectra measured at different temperatures for all three samples,

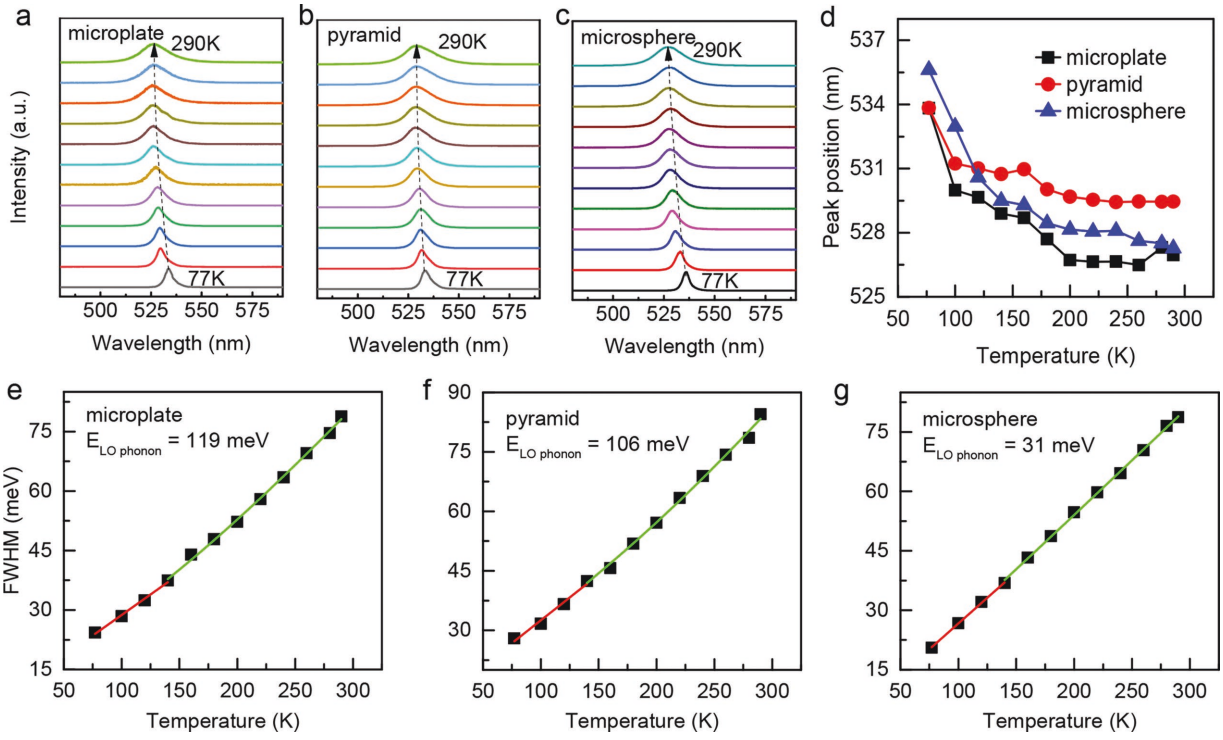


**Figure 3.** Temperature-dependent PL spectra of a) microplates, b) pyramids, and c) microspheres with diameter of ≈2 µm. d) PL peak positions of microplates (black dots), pyramids (red dots), and microspheres with diameter of ≈2 µm (blue dots) versus temperature extracted from spectra (a–c). Full width at half maximum (FWHM) of e) microplates, f) pyramids, and g) microspheres with diameter of ≈2 µm versus temperature extracted from panels (a–c). The solid red and green lines are the fittings according to $\Gamma(T) = \Gamma_{inh} + \gamma_{ph}T$ and Equation (2), respectively.

and the emission peak gradually blue shifts with the increase of the temperature. This trend is much clear if we extracted peak positions from these spectra and plotted against temperature as shown in Figure 3d. The blue-shift of peak position with increasing temperature is consistent with previous studies.[26] Nevertheless, the decreasing rate of the PL peak positions is gradually slowed down above ≈180 K for all morphologies, which can be ascribed to the combining contribution of the thermal expansion (TE) and electron–phonon (EP) coupling to the band gap.[26] By assuming a linear relationship between lattice constant and temperature, the temperature ($T$)-dependent band gap $E_g$ can be described by the following equation[26]

$$E_g(T) = E_0 + A_{TE}T + A_{EP}\left(\frac{2}{\exp(\hbar\omega/k_BT)-1}+1\right) \quad (1)$$

where $A_{TE}$ and $A_{EP}$ are the weight of the TE and EP interaction, and $\hbar\omega$ is the optical phonon energy. $E_0$ is the unrenormalized band gap, $E_g(T=0) = E_0 + A_{EP}$ and $k_B$ is the Boltzmann constant. This equation clearly shows that the TE interaction mainly contributes to the increased band gap in the low-temperature regime. Therefore, the peak position linearly decreases with temperature below ≈180 K. The EP interaction starts to play a role in the high-temperature regime. The negative $A_{EP}$ leads to a negative contribution to the band gap with the increase of the temperature, resulting in the decrease of the increasing rate of the PL peak position above ≈180 K.

To investigate how the phases and morphologies influence the electron–phonon interaction, the temperature-dependent FWHMs is extracted from PL spectra (Figure 3e–g). The trend of FWHMs with temperature for all morphologies agrees well with the previous reports.[26] The temperature-dependent FWHMs can be approximately expressed by

$$\Gamma(T) = \Gamma_{inh} + \gamma_{ph}T + \frac{\Gamma_{LO}}{\left[\exp(\hbar\omega_{LO}/k_BT)-1\right]} \quad (2)$$

where $\Gamma_{inh}$, $\gamma_{ph}$, $\Gamma_{LO}$, and $\hbar\omega_{LO}$ represent the inhomogeneous PL peak broadening at 0 K, the coupling strength of exciton–acoustic phonon, the coupling strength of exciton–LO phonon, and the LO-phonon energy, respectively. This equation unambiguously shows that exciton–acoustic phonon coupling (the second term) dominates the broadening FWHM at lower temperatures while the exciton–LO phonon interaction starts to play a role at higher temperatures.[27] As shown in Figure 3e–g, for $T < 140$ K the FWHMs versus temperature can be well fitted by $\Gamma(T) = \Gamma_{inh} + \gamma_{ph}T$. For $T > 140$ K, the exciton–LO phonon coupling cannot be ignored anymore and thus Equation (2) gives a better fitting. The fitting results indicate that the LO phonon energy of microspheres is 31 meV, much lower than those of microplates and pyramids (119 and 106 meV, respectively). We measured a few samples and for all samples the phonon energy in microspheres is much smaller than that of microplates and pyramids (Figure S2, Supporting Information). It should be noted that the LO phonon energy obtained via fitting is the average energy contributing to the broadening. Similar to CdSe/CdS core–shell quantum dots, the presence of the CdS shell layer can greatly alter the exciton–phonon coupling

strength and the average phonon energy due to the change of the localization volume of the exciton and the different phonon participating to the interaction.[28] In our cases, compared with that of $CsPbBr_3$ (2.88 Å),[29] $Cs_4PbBr_6$ (3.03 Å) has a larger bond distance leading to a lower LO phonon energy.[30] The vibronic levels in the $CsPbBr_3$ are less populated compared with that in $Cs_4PbBr_6$ due to the lower phonon energy, resulting in the lower average phonon energy we obtained. Finally, the low average phonon energy in microspheres gives rise to a weaker interaction among atoms and thus a much lower LO-phonon energy.[31] The much lower LO-phonon energy in $CsPbBr_3$ microspheres implies a lower phonon-disturbance to carriers, favoring to reduce the rate of nonradiative transition and thus enhanced PL intensity.[31] Therefore, the presence of $Cs_4PbBr_6$ would be beneficial to, rather than deteriorating the PL efficiency.

In additional to the low average phonon energy, the energy band alignment between $Cs_4PbBr_6$ and $CsPbBr_3$ also favors the enhancement of $CsPbBr_3$ emission. According to the band structure by density functional theory, the energy levels of $Cs_4PbBr_6$ are much deeper than those of $CsPbBr_3$ (conduction band −3.33 eV, valence band −5.67 eV), indicating that $Cs_4PbBr_6$ layer can act as a blocking wall to limit the photogenerated carriers diffusion within $CsPbBr_3$ (Figure S3, Supporting Information).[32] This is helpful to increase the luminescence yield since the diffusion length of carriers is reduced and the radiative recombination is thus enhanced. Furthermore, the microspheres are polycrystals and thus the size of the $CsPbBr_3$ grains might be small and the grains are passivated by the surrounding $Cs_4PbBr_6$, both of which are also beneficial for the high PLQYs. Those three factors might together enhance the PL efficiency in microspheres, in spite of their polycrystalline nature.

The significant improvement of the PL efficiency in $CsPbBr_3$ microspheres inspires us to tune the emission wavelength in order to fill the so-called "green gap" for backlighting display. This can be achieved via tuning the diameter of the microspheres by placing the substrate at different distance from the position of the precursor. The diameter of the resultant microspheres monotonously decreases from 50 to 2 μm as the distance increases from 10 to 12.5 cm (**Figure 4**a–e). The histogram to describe the size distribution of microspheres is shown in Figure 4f. The room-temperature PL spectra and the extracted peak positions of as-synthesized microspheres with various diameters are shown in Figure 4g,i, respectively. The PL peak positions red-shift from 527 to 539 nm with all FWHMs smaller than 20 nm when the diameter of the microspheres increases from 2 to 50 μm. It should be noted that the largest size of microsphere we can grow is ≈50 μm, corresponding to the emission peak of ≈539 nm. We tried to change the growth conditions such as placing the substrate on 9.5 cm or closer of the tube furnace to obtain microspheres with a larger size. However, the synthesized microspheres were cracked probably due to the high temperature annealing (Figure S4, Supporting Information).

The red-shift of the emission peak with increasing diameters might be attributed to the reabsorption effect.[33] Due to the presence of the thermal broadening of energy bands, the energy band tails extend into the energy gap (Urbach tail).[34] Therefore, the emitted photons can be reabsorbed by the band tail states and lower energy photons are re-emitted. Each of this reabsorption processes reduces the photon energy and thus leads to the redshift of the emission peak. The number of the reabsorption cycles increases with the increasing diameter of microspheres, resulting in a larger red-shift of peak positions for a larger microsphere. Since the thermal broadening of energy bands would be reduced as the temperature decreases, the reabsorption effect would decrease or even disappear at a lower temperature. Indeed, at 77 K the peak shift is greatly reduced with the increase of the diameter compared with that at room temperature (Figure 4h,i).

To further verify that the reabsorption effect leads to the redshift of the emission peak, we have compared the temperature-dependent PL peak of a 10 μm microsphere with that of a 2 μm microsphere. With a larger diameter, the reabsorption effect is expected to be much stronger in the 10 μm microsphere. If the reabsorption effect is reduced, the difference of the peak position of those two microspheres should decrease or even vanish at a reduced temperature. Indeed, we observed a reduced redshift or even no redshift of emission peak positions as the temperature decreases (Figure 4j), suggesting this redshift is indeed due to the reabsorption effect. It should be noted that the microspheres are polycrystals according to the SEM images and optical images. Therefore, the grain size may vary with the diameter of the microspheres, which would lead to the change of PL emission. If the grain size is small enough that the quantum confinement effect takes place, a blueshift of the PL peak should be observed. Nevertheless, the quantum confinement effect should not strongly depend on the temperature. Therefore, this blueshift cannot be due to the quantum confinement effect according to our observed results (Figure 4i).

The continuous tunability of the emission peak position from 527 to 539 nm by changing the diameter of microspheres renders the $CsPbBr_3$ microspheres to be an ideal candidate for the pure green emitter with high PLQY. To check how the PLQYs depends on the diameter of the microspheres, we have measured the PLQYs of $CsPbBr_3$ microspheres with various diameters. We have also summarized the PLQYs of $CsPbBr_3$ microplates, pyramids, and microspheres with different diameters as shown in Figure 4k. Within the experimental errors, the PLQYs of microspheres can be as high as 75% for all microspheres and shows no apparent size dependence. This is the highest PLQYs for perovskite-based pure green emitters up to date (Table S1, Supporting Information).[16,17,36] In addition, PL mapping image indicates that the emission is rather uniform for the entire microsphere even at the area close to the edge (Figure S5, Supporting Information). All those factors favor that our $CsPbBr_3$ microspheres would be very promising for pure green emitters.

Understanding the growth mechanism can help efficiently control the growth of microspheres with a desirable diameter for the backlighting displays. The growth of the microspheres with various diameters is achieved via tuning the growth rate by controlling the distance between the deposition position and precursor. Following the previously reported two-dimensional diffusion model[35] (**Figure 5**a), the calculated growth rate can be written as

$$\dot{G}(x) = -\frac{M_{\text{products}}}{\rho_{\text{products}} M_{\text{precursors}}} J(x) = \frac{DC_i M_{\text{products}}}{b\rho_{\text{products}} M_{\text{precursors}}} \exp\left(-\frac{\pi^2 Dx}{4\vec{v}b^2}\right) \text{cm/sec} \quad (3)$$

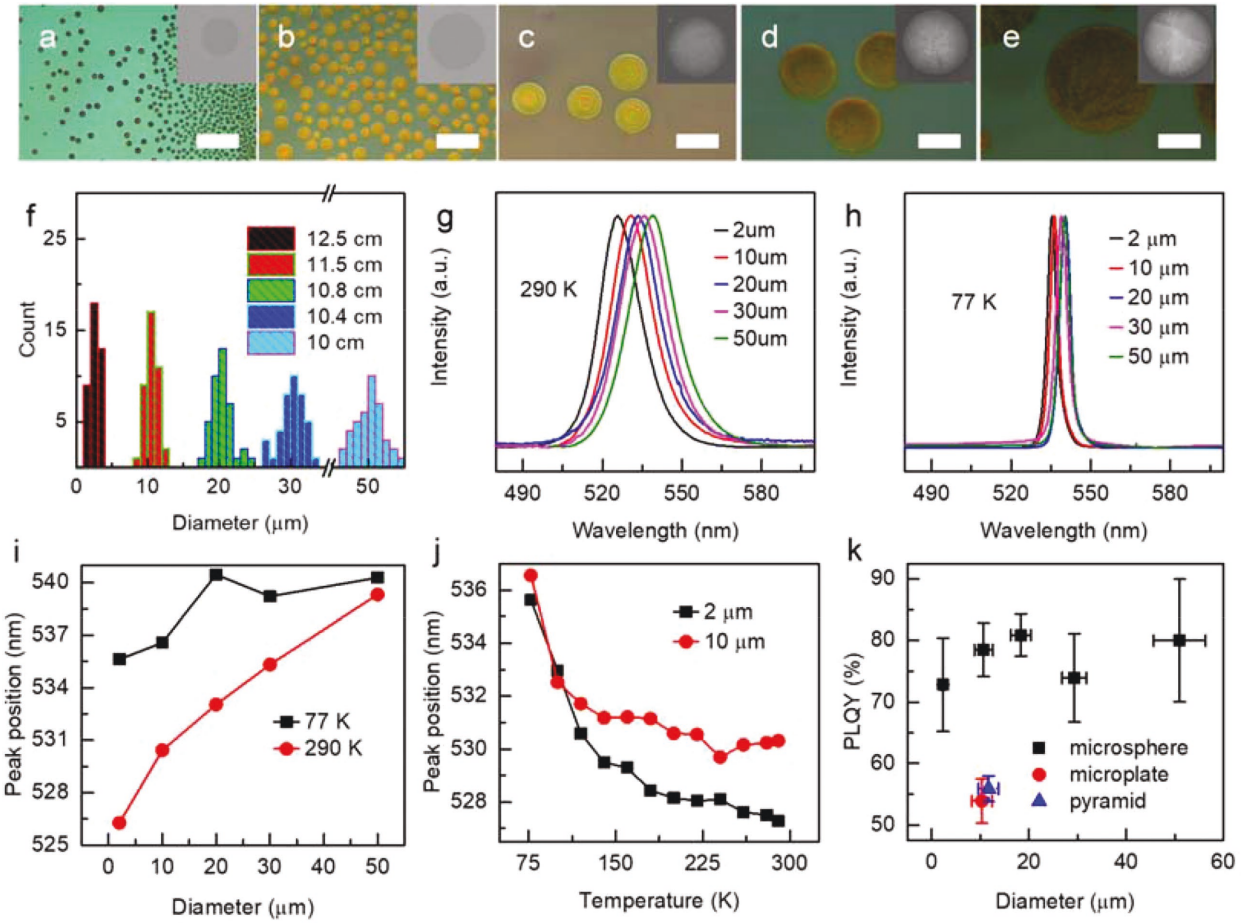


**Figure 4.** Optical and SEM images of microspheres with diameters of a) 2 μm, b) 10 μm, c) 20 μm, d) 30 μm, and e) 50 μm, which are deposited on 12.5, 11.5, 10.8, 10.4, and 10 cm of the tuber furnace. The scale bar is 30 μm for all optical images. f) Histogram of diameters on the different distances between the deposition position and precursor. g–h) The PL spectra of microspheres with diameters ranging from 2 to 50 μm at g) room-temperature and at h) 77 K. i) The diameter dependent PL peak positions at room-temperature (red dots) and at 77 K (black dots) extracted from panels (g) and (h). The emission peak shows a red-shift from 527 to 539 nm and from 536 to 540 nm with diameters increasing from 2 to 50 μm, respectively. j) Temperature dependent PL peak positions of microspheres with diameters of 2 μm (black dots) and 10 μm (red dots). k) The measured PLQYs of microplates (red dots), pyramids (blue dots), and microspheres (black dots) with various diameters.

where $M_{products}$, $M_{precursors}$, $\rho_{products}$, $J(x)$, $D$, $C_i$, $\overline{v}$, and $b$ are the molecular weight of target products ($CsPbBr_3/Cs_4PbBr_6$), the molecular weight of precursors ($CsBr/PbBr_2$), the density of target products, the mass flux of precursors, diffusivity, the concentration of source at $x = 0$, drift velocity, and the depth of the quartz boat. Equation (3) indicates that the growth rate decreases exponentially with the increase of the distance $x$ between the deposition position and precursor. The extracted

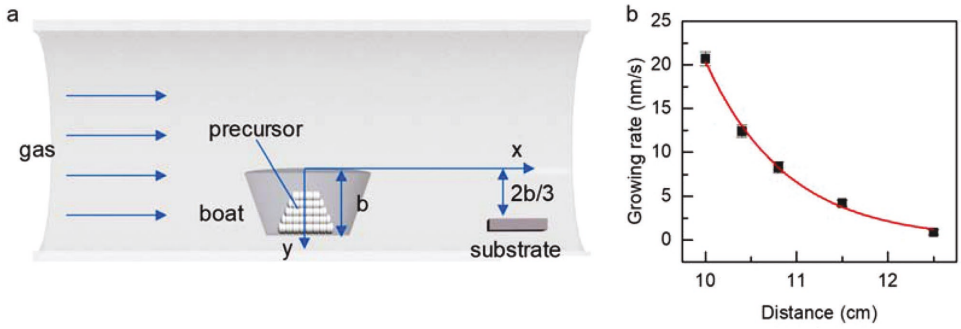


**Figure 5.** a) The schematic diagram of the 2D diffusion model. b) The distance dependent growth rate of microspheres. The black square dots are the experimental results and the solid red line is the fit according to $y = 2086 \times \exp(-1.15 \times x)$.

growth rate, defined as the ratio of the diameter of microspheres to the growth time, agrees well with the calculated one (Figure 5b), verifying that the diameter of the microspheres is indeed controlled by the growth rate according to the 2D diffusion model.

## 3. Conclusions

We report on vapor-phase growth of $CsPbBr_3$ microstructures for highly efficient pure green light emission. We have synthesized $CsPbBr_3$ microplates, pyramids, and microspheres by properly controlling the cooling rate of the tube furnace and the growth time. The PL intensity of microspheres is higher than those of microplates and pyramids which might be due to the lower phonon disturbance to carriers caused by the lower LO-phonon energy and the band alignment between $CsPbBr_3$ and $Cs_4PbBr_6$. The diameter of microspheres can be monotonously tuned from 2 to 50 μm via controlling the growth rate based on the 2D diffusion model. This tunability of the diameter of microspheres results in the continuously red-shifting of the PL peak position from 527 to 539 nm because of the reabsorption effect, which can well fill the so-called "green gap." In particular, the PLQYs of microspheres with pure green emission can achieve as high as 75%, which is the highest number for the pure green light emission of perovskites. Our studies not only can help understand the critical role for improving the emission efficiency, but provide an alternative approach to fill the so-called "green gap" based on $CsPbBr_3$ and thus open the way toward realization of the pure green light emission for the low-cost backlighting display.

## 4. Experimental Section

*Sample Preparation*: $CsPbBr_3$ microstructures were grown by a vapor phase method using a home-built chemical vapor deposition system. The precleaned Si substrate was placed in the downstream of a quartz tube mounted in a single zone furnace (Lindberg/Blue MTF55035KC-1) with the distance of ≈10 cm between the substrate Si and the center of the tube furnace. The mixed powder of CsBr and $PbBr_2$ with the molar ratio of 1:1 was put at the center of the tube furnace. After the tube was pumped down to a pressure of 2 mTorr and then purged with a flow of Ar gas for several times, the furnace was heated to ≈570 °C with a carrier argon gas at a flow rate of 100 sccm. For microplates and pyramids, the growth time was set to be 5 min while the lid of the furnace was opened at 500 and 300 °C, respectively. For microspheres, the growth time was prolonged to be 40 min and the lid of the furnace was opened at 300 °C. The tube furnace was naturally cooled down to room temperature when the argon gas flow was maintained.

*Material Characterizations*: Optical and SEM images were acquired by a Mshot-MJ30 optical microscope and a tungsten filament scanning electron microscope (TESCAN VEGA 3 SBH). PXRD measurements were carried out using a Bruker D2 PHPSER (Cu K$\alpha$ $\lambda$ = 0.15419 nm, Nickel filter, 25 kV, 40 mA). The room-temperature PL measurements were carried out on a home-built micro-Raman spectrometer (Horiba JY iHR550 spectrometer) in a backscattering configuration excited by a 405 nm laser with a power of 2 μW. The temperature dependent PL studies were performed in the same configuration coupled with a vacuum liquid helium continues flow cryostat (Cryo Industry of America, USA) and the temperature was controlled via a temperature controller (Lake Shore Model 336). The PLQYs were measured at the same setup by using CdSe quantum dot films to calibrate the system. The reflection measurements were conducted in the same setup and a halogen lamp was used as the light source.

## Supporting Information

Supporting Information is available from the Wiley Online Library or from the author.

## Acknowledgements

D.L. acknowledges the support from NSFC (61674060) and the Fundamental Research Funds for the Central Universities, HUST (2017KFYXJJ030, 2017KFXKJC002, 2017KFXKJC003, 2018KFYXKJC016) and National Young 1000 Talent Plan of China. H.L. thanks the support from New Mexico EPSCoR with NSF-1301346. The authors thank Hong Cheng engineer in the Analytical and Testing Center of Huazhong University of Science and Technology for the support in PL measurement and thank the Center of Micro-Fabrication of WNLO for the support in XRD measurement.

## Conflict of Interest

The authors declare no conflict of interest.

## Keywords

$CsPbBr_3$, LO phonon, microspheres, pure green emission, reabsorption

Received: October 2, 2018
Revised: October 26, 2018
Published online:

[1] G. Wang, D. Li, H.-C. Cheng, Y. Li, C.-Y. Chen, A. Yin, Z. Zhao, Z. Lin, H. Wu, Q. He, M. Ding, Y. Liu, Y. Huang, X. Duan, *Sci. Adv.* **2015**, *1*, e1500613.
[2] Q. Dong, Y. Fang, Y. Shao, P. Mulligan, J. Qiu, L. Cao, J. Huang, *Science* **2015**, *347*, 6225.
[3] H. Oga, A. Saeki, Y. Ogomi, S. Hayase, S. Seki, *J. Am. Chem. Soc.* **2014**, *136*, 13818.
[4] Z. Xiao, R. A. Kerner, L. Zhao, N. L. Tran, K. M. Lee, T.-W. Koh, G. D. Scholes, B. P. Rand, *Nat. Photon.* **2017**, *11*, 108.
[5] K. X. Steirer, P. Schulz, G. Teeter, V. Stevanovic, M. Yang, K. Zhu, J. J. Berry, *ACS Energy Lett.* **2016**, *1*, 360.
[6] W. S. Yang, B.-W. Park, E. H. Jung, N. J. Jeon, Y. C. Kim, D. U. Lee, S. S. Shin, J. Seo, E. K. Kim, J. H. Noh, S. I. Seok, *Science* **2017**, *356*, 1376.
[7] X. Hu, X. Zhang, L. Liang, J. Bao, S. Li, W. Yang, Y. Xie, *Adv. Funct. Mater.* **2014**, *24*, 7373.
[8] Y. Jia, R. A. Kerner, A. J. Grede, B. P. Rand, N. C. Giebink, *Nat. Photon.* **2017**, *11*, 784.
[9] M. Kulbak, S. Gupta, N. Kedem, I. Levine, T. Bendikov, G. Hodes, D. Cahen, *J. Phys. Chem. Lett.* **2016**, *7*, 167.
[10] R. J. Sutton, G. E. Eperon, L. Miranda, E. S. Parrott, B. A. Kamino, J. B. Patel, M. T. Hörantner, M. B. Johnston, A. A. Haghighirad, D. T. Moore, H. J. Snaith, *Adv. Energy Mater.* **2016**, *6*, 1502458.
[11] M. I. Saidaminov, M. A. Haque, J. Almutlaq, S. Sarmah, X.-H. Miao, R. Begum, A. A. Zhumekenov, I. Dursun, N. Cho, B. Murali,

 

O. F. Mohammed, T. Wu, O. M. Bakr, *Adv. Opt. Mater.* **2017**, *5*, 1600704.
[12] J. Li, L. Xu, T. Wang, J. Song, J. Chen, J. Xue, Y. Dong, B. Cai, Q. Shan, B. Han, H. Zeng, *Adv. Mater.* **2017**, *29*, 1603885.
[13] Y. Wang, X. Li, J. Song, L. Xiao, H. Zeng, H. Sun, *Adv. Mater.* **2015**, *27*, 7101.
[14] H.-C. Wang, S.-Y. Lin, A.-C. Tang, B. P. Singh, H.-C. Tong, C.-Y. Chen, Y.-C. Lee, T.-L. Tsai, R.-S. Liu, *Angew. Chem., Int. Ed.* **2016**, *55*, 7924.
[15] C.-M. Chang, Y.-C. Fang, C.-R. Lee, A new design mixing RGB LED (red, green, blue light-emitting diode) for a modern LCD (liquid crystal display) backlight system, in *Nonimaging Optics and Efficient Illumination Systems III*, IEEE Proc. Vol. 6338 (Eds: R. Winston, P. Benítez), San Diego, September, **2006**.
[16] D. Yu, F. Cao, Y. Gao, Y. Xiong, H. Zeng, *Adv. Funct. Mater.* **2018**, *28*, 1800248.
[17] Y. Tong, E.-P. Yao, A. Manzi, E. Bladt, K. Wang, M. Doblinger, S. Bals, P. Muller-Buschbaum, A. S. Urban, L. Polavarapu, J. Feldmann, *Adv. Mater.* **2018**, *30*, 1801117.
[18] Q. Zhang, R. Su, X. Liu, J. Xing, T. C. Sum, Q. Xiong, *Adv. Funct. Mater.* **2016**, *26*, 6238.
[19] Y. Wang, X. Guan, D. Li, H.-C. Cheng, X. Duan, Z. Lin, X. Duan, *Nano Res.* **2017**, *10*, 1223.
[20] S. Hirotsu, J. Harada, M. Iizumi, K. Gesi, *J. Phys. Soc. Jpn.* **1974**, *37*, 1393.
[21] T. Baikie, Y. Fang, J. M. Kadro, M. Schreyer, F. Wei, S. G. Mhaisalkar, M. Graetzel, T. J. White, *J. Mater. Chem. A* **2013**, *1*, 5628.
[22] H. Bloom, M. White, *Aust. J. Chem.* **1981**, *34*, 479.
[23] K. Heidrich, W. Schäfer, M. Schreiber, J. Söchtig, G. Trendel, J. Treusch, T. Grandke, H. J. Stolz, *Phys. Rev. B* **1981**, *24*, 5642.
[24] J. Shamsi, Z. Dang, P. Bianchini, C. Canale, F. D. Stasio, R. Brescia, M. Prato, L. Manna, *J. Am. Chem. Soc.* **2016**, *138*, 7240.
[25] M. Imran, F. D. Stasio, Z. Dang, C. Canale, A. H. Khan, J. Shamsi, R. Brescia, M. Prato, L. Manna, *Chem. Mater.* **2016**, *28*, 6450.
[26] K. Wei, Z. Xu, R. Chen, X. Zheng, X. Cheng, T. Jiang, *Opt. Lett.* **2016**, *41*, 3821.
[27] A. D. Wright, C. Verdi, R. L. Milot, G. E. Eperon, M. A. Perez-Osorio, H. J. Snaith, F. Giustino, M. B. Johnston, L. M. Herz, *Nat. Commun.* **2016**, *7*, 11755.
[28] A. W. Achtstein, O. Marquardt, R. Scott, M. Ibrahim, T. Riedl, A. V. Prudnikau, A. Antanovich, N. Owschimikow, J. K. N. Lindner, M. Artemyev, U. Woggon, *ACS Nano* **2018**, *12*, 9476.
[29] P. Cottingham, R. L. Brutchey, *Chem. Commun.* **2016**, *52*, 5246.
[30] M. Velázquez, A. Ferrier, S. Péchev, P. Gravereau, J.-P. Chaminade, X. Portier, R. Moncorgé, *J. Cryst. Growth* **2008**, *310*, 5458.
[31] X. Li, Y. Wu, S. Zhang, B. Cai, Y. Gu, J. Song, H. Zeng, *Adv. Funct. Mater.* **2016**, *26*, 2435.
[32] Y. Shang, G. Li, W. Liu, Z. Ning, *Adv. Funct. Mater.* **2018**, *28*, 1801193.
[33] A. Pan, D. Liu, R. Liu, R. Wang, X. Zhu, B. Zou, *Small* **2005**, *1*, 980.
[34] S. Yakunin, L. Protesescu, F. Krieg, M. I. Bodnarchuk, G. Nedelcu, M. Humer, G. D. Luca, M. Fiebig, W. Heiss, M. V. Kovalenko, *Nat. Commun.* **2015**, *6*, 8056.
[35] J. Zhou, J. Lin, X. Huang, Y. Zhou, Y. Chen, J. Xia, H. Wang, Y. Xie, H. Yu, J. Lei, D. Wu, F. Liu, Q. Fu, Q. Zeng, C.-H. Hsu, C. Yang, L. Lu, T. Yu, Z. Shen, H. Lin, B. I. Yakobson, Q. Liu, K. Suenaga, G. Liu, Z. Liu, *Nature* **2018**, *556*, 355.
[36] L. Protesescu, S. Yakunin, M. I. Bodnarchuk, F. Krieg, R. Caputo, C. H. Hendon, R. X. Yang, A. Walsh, M. V. Kovalenko, *Nano Lett.* **2015**, *15*, 3692.